1 **Heteroatom-doped graphene aerogels and carbon-magnetite catalysts for the**

2 **heterogeneous electro-Fenton degradation of acetaminophen in aqueous solution**

3 Nerea Fernández-Sáez,[a] Diana E. Villela-Martinez, [a,b] Francisco Carrasco-Marín,[a] Agustín F.

4 Pérez-Cadenas,[a] Luisa M. Pastrana-Martínez*[a]

5 [a] *Carbon Materials Research Group, Department of Inorganic Chemistry, Faculty of Sciences,*

6 *University of Granada, Avenida de Fuentenueva, s/n., ES18071 Granada, Spain.*

7 [b] *Centro de Investigación y Estudios de Posgrado, Facultad de Ciencias Químicas, Universidad*

8 *Autónoma de San Luis Potosí, San Luis Potosí, Mexico*

9

10 *Corresponding author e-mail address: lpastrana@ugr.es (L.M. Pastrana-Martínez)

11 Tel: +34-958240443

12

13

14

15

16

17

18

19

20

21

22

23

24

25

Abstract

Nitrogen (N) and nitrogen/sulphur (N/S) co-doped graphene aerogels were synthesized by hydrothermal method using graphene oxide and urea or thiourea as precursors following a freezing-drying process. The determination of the number of the electrons involved in the mechanism of electro-reduction of oxygen (ORR) in alkaline medium was assessed. The mechanism of $4e^-$ was obtained with N/S-doped graphene aerogels showing good electrocatalytic behavior and larger kinetic current densities. The $2e^-$ ORR process (involving in situ H_2O_2 generation) was mainly obtained using N-doped graphene aerogels and it was related to the content of N functionalities as well as to the porous texture of the samples. Carbon-magnetic catalyst was synthesized to promote the decomposition of H_2O_2 to $HO^{\bullet}$ for the degradation of acetaminophen (ACE) in heterogeneous electro-Fenton (EF) process. The highest pollutant removal (71.0%) and mineralization (51.6%) were obtained with N-doped materials and carbon-Fe_3O_4 catalyst, showing good stability and low iron leaching (0.33 mg L^{-1}).

50

1. Introduction

Water pollution is an immediate consequence of population growth, agricultural and industrial expansion and is on the limit of a critical point in several zones of the globe. Pharmaceutical compounds have been found not only in the sea but also in tap water [1], with the direct damage in worldwide public health [2, 3]. Acetaminophen (ACE, also known as paracetamol) whose chemical name is *N*-acetyl-*p*-aminophenol, is one of the most present drugs found on waste water [1, 4, 5] due to aspects as poor removal efficiency [6] or toxic impact on the environment [7]. ACE is one of the most commonly used analgesics with and without prescription and has a great impact in the health causing liver injury, hepatocyte necrosis and even mortality. Among 58-68% of the molecule is excreted from the body and finishes in municipal waste system [8]. In the last few decades, advanced oxidation processes (AOPs), including chemistry, photochemistry, photocatalytic, electrochemistry and photo-electrochemistry methods have been developed as powerful and environmentally-friendly technologies for the complete decomposition of organic contaminants [9]. AOPs consist on the generation of highly reactive species, mainly hydroxyl radicals (HO$^{\bullet}$) [10, 11] being possible to obtain the complete mineralization of organic pollutants into H_2O, CO_2 and inorganic ions. Among the AOPs, the Fenton-based process has become an ideal method because of its high performance and easy operation. The classical Fenton process involves the production of HO$^{\bullet}$ radicals from hydrogen peroxide (H_2O_2) and Fe^{2+} or Fe^{3+} ions at acidic pH values (2.5-3.0) [12], following the Eq. 1 [13]:

$$Fe^{2+} + H_2O_2 + H^+ \rightarrow Fe^{3+} + HO^{\bullet} + H_2O \tag{1}$$

One of the ecofriendly and more cost-effective versions of this kind of process, is the electro-Fenton (EF) process. This technology is based on the electrochemical generation of HO$^{\bullet}$ radicals through (i) the *in situ* electrogeneration of H_2O_2 at the cathode by oxygen reduction

75   reaction (ORR) which mainly consists of 2e⁻ process (Eq. 2) instead 4 e⁻ process that generate

76   H_2O (Eq. 3); (ii) the addition of Fe^{2+} catalyst to the solution and (iii) the continuous regeneration

77   of Fe^{3+} to Fe^{2+} at the cathode [14].

78    $$O_2 + 2H^+ + 2e^- \rightarrow H_2O_2 \tag{2}$$

79    $$O_2 + 4H^+ + 4e^- \rightarrow 2H_2O \tag{3}$$

80   It well known that various carbon-based materials such as carbon fiber [15], carbon black [16],

81   carbon nanotubes [17] and graphene [18], among others, have been suggested interesting

82   alternatives to precious metals as cathode for EF process because of their nontoxicity, excellent

83   conductivity, good stability and low cost. Graphene derivatives (e.g., graphene oxide, GO and

84   reduced graphene oxide, rGO) and more recently three-dimensional (3D) graphene-based

85   aerogel [19] have been investigated as ORR catalysts in alkaline electrolytes due to its large

86   specific surface area, high electrical conductivity, mechanical strength, easy functionalization

87   [20] and multiplex electron transfer pathways [21]. It is noteworthy that the presence of

88   heteroatoms atoms such as O, N, B, P, and S, as well as defect sites on the lattice of graphene

89   would influence the adsorption of O_2, enhancing ORR activity [22-25].

90   Heterogeneous EF process normally uses solid catalyst source such iron species (or transition

91   metals) supported on a porous matrix for the decomposition of H_2O_2 to $HO^\bullet$ radicals. In this

92   regard, several materials have been reported as catalyst supports, i.e. ionic exchange resins,

93   silicates and carbon-based materials, among others [26]. Activated carbon is one of the most

94   interesting catalyst support due to its low cost as well as textural, chemical and morphological

95   tunable properties, which can play a significant role during the degradation of organic pollutants

96   [27, 28].

97   Heterogeneous mode unravel the problem associated with the generation of sludge, which

98   should be eliminated by costly processes [29]. In this sense, the utilization of magnetic catalyst

99   has been reported as an easier and efficient way of catalyst recovery under a magnetic field,

100 showing reusability properties [30]. Although the use of iron supported on activated carbon has

101 been previously reported as catalyst in EF reaction for the degradation of several pollutants,

102 such as phenol [28] or methyl blue [31], to the best of our knowledge there are no works in

103 literature using both heteroatom-doped graphene aerogels and magnetic carbon-iron oxide

104 particles in the heterogeneous electro-Fenton degradation of acetaminophen in aqueous

105 solution.

106 In view of these precedents, the aim of this work is to study the potential of N- and N/S-doped

107 graphene aerogels as cathode in oxygen reduction reaction and evaluate the electrons involved

108 in the process; i.e. 4 or 2 electrons for H_2O or H_2O_2 generation, respectively. The effect of N

109 or N/S species on ORR activity will be also discussed. Carbon-Fe_3O_4 catalysts are used to

110 promote the decomposition of H_2O_2 to $HO^\bullet$ radicals for the sake of improving both conversion

111 and mineralization of ACE in heterogeneous electro-Fenton process.

112

113 **2. Materials and methods**

114 *2.1.Chemicals*

115 Graphite powder < 20 µm, acetaminophen, ACE ($C_8H_9NO_2$, Mr 151,163 g mol^{-1}, 99.5 wt.%

116 [CAS number: 103-90-2]) and formaldehyde (99.5%) were purchased from Sigma-Aldrich.

117 Sulphuric acid (H_2SO_4, 95-98%) and potassium permanganate ($KMnO_4$, 99.0%) were obtained

118 from PanReac AppliChem. Sodium nitrate ($NaNO_3$, >99.0%), urea (NH_2CONH_2, 99.5%) and

119 thiourea (CH_4N_2S, 99%) from Alfa Aesar. *Tert*-butanol ($C_4H_{10}O$) was obtained from Fluka.

120

121 *2.2.Synthesis of graphene oxide (GO)*

122 GO was synthesized from synthetic graphite (powder, particle size < 20 µm) by a modified

123 Hummers method [32, 33] described elsewhere [33]. The resultant material was dispersed in

124 distilled water (2g L^{-1}) and sonicated in an ultrasound bath for one hour. After that, the

125 unexfoliated graphite oxide was removed by centrifugation (20 min at 3000 rpm).

126

127

2.3. Synthesis of N and S-doped graphene aerogels

N-doped graphene and N/S-doped graphene aerogels were obtained by hydrothermal reduction

of GO suspension (1.3 g/L) with urea [34] or thiourea as N or N/S precursor, respectively. In a

typical procedure, the appropriate amount of urea or thiourea was dissolved in 60 mL of GO

suspension and transferred into a 100 mL Teflon autoclave and subjected to hydrothermal

treatment at 180°C for 12h. The as-prepared resultant sponge was immersed in distilled water

for 4 days to remove residues. Then, the graphene-based material was placed in acetone for 3

days making an acetone changing twice a day. Subsequently, the solid was filtered and placed

on tert-butanol and finally the solvent was eliminated by freeze drying. The materials were

labelled as rGO-N-X or rGO-N/S-X when using urea or thiourea as precursors, respectively

where X refers to the ratio GO:precursor (i.e. 5, 10 and 20 for 1:5, 1:10 and 1:20 ratio of

GO:urea or GO:thiourea, respectively). For the comparison purpose, the rGO aerogel was also

synthetized via the same procedure without the addition of urea or thiourea.

141

2.4. Synthesis of magnetite and carbon-magnetite

The iron oxide (Fe_3O_4) magnetic particles were synthesized by the method previously described

by Petcharoen and Sirivar [35]. In a typical procedure, 1.5g of $FeCl_2$ and 3g of $FeCl_3$ (molar

relation of 2; Fe^{3+}/Fe^{2+} in solution) were dissolved in 100 mL of distilled water under N_2 flow

with vigorous stirring, then 10 mL of NH_4OH at 25% was added to the resultant mixture

producing a color change from orange to black. The magnetic particles precipitated were

washed with deionized water, ethanol and dried at 80°C for 8 hours. The iron oxide particles

will be denoted as Fe_3O_4.

Carbon-magnetite composite was prepared using a mix of resorcinol-formaldehyde as the

carbon source. In a typical procedure, a solution of the obtained Fe_3O_4 in 50 mL of NH_4OH

152 (30%) was added to 500 mL of n-heptane with a stirring of 450 rpm and heated at 70°C. The

153 amount of magnetite was calculated according 10% of final weight of carbon gel. A solution of

154 resorcinol (R), formaldehyde (F) and water (W) in proportion R/F=1 and R/W=2 (containing

155 25g of R, 45 mL of F and 58 mL of W), was added dropwise to de Fe_3O_4/n-heptane solution.

156 The resultant gel was aged at 70°C for 24 h under stirring. After that, the suspension formed

157 was filtered and the solid placed in acetone for 2 days [36] making an acetone changing twice

158 a day in order to reduce porosity collapse with the following drying step [37]. After 2 days in

159 acetone the solid was filtered and placed on tert-butanol, the solvent was eliminated by freeze

160 drying. The obtained material was treated in a furnace with N_2 flow at 2 °C min^{-1} until 900°C

161 and with soak time of 2 h. The carbon-magnetite composite is referred as carbon-Fe_3O_4.

162

163   *2.5.Characterization techniques*

164 Textural characterization was carried out by N_2 adsorption at −196 °C, using a Quantachrome

165 Autosorb-1 equipment. The BET and Dubinin–Radushkevich equations were applied to

166 determine the apparent surface area (S_{BET}) and the micropore volume (W_0) and the mean

167 micropore width (L_0), respectively. Pore size distributions were obtained by applying the

168 Barret-Joyner-Hallender (BJH) method. The mesopore volume of the samples (V_{mes}) were

169 obtained from the volume of N_2 adsorbed at $P/P_0 = 0.95$ and the micropore volume (W_0). The

170 chemical characterization of the composites was further analyzed by X-ray photoelectron

171 spectroscopy (XPS). The spectra were obtained on a Kratos Axis Ultra-DLD X-ray

172 photoelectron spectrometer equipped with a hemispherical electron analyzer operating at 12 kV

173 and 10 mA connected to a detector DLD (delay-line detector). Raman spectra were obtained

174 using a Micro-Raman JASCO NRS-5100 dispersive spectrometer with a 532 nm laser line.

175 Attenuated total reflection Fourier transform infrared (ATR-FTIR) spectra were recorded on a

176 NICOLET 510P spectrometer using ZeSn as ATR crystal. The total oxygen content of samples

177 was obtained with an elemental CHNS-O Analyzer Flask (1112 Series) from Thermo Finigan.

178 The morphology of the materials was analyzed by scanning electron microscopy (SEM) using

179 a LEO (Carl Zeiss) GEMINI-1530 microscope. Transmission electron microscopy (TEM) was

180 performed in a LIBRA 120 PLUS (Carl Zeiss) equipment. The iron oxide phase and

181 crystallinity were determined by a powder X-ray diffraction (XRD) pattern using a Bruker D8

182 Advance X-ray diffractometer equipped with Cu Ka radiation at a wavelength (λ) of 1.541 Å.

183

184 *2.6.Electrochemical characterization*

185 To test the oxygen reduction activity of the graphene-based aerogels, cyclic voltammetry (CV)

186 and linear sweep voltammetry (LSV) experiments were carried out in a three-electrode cell

187 controlled by a Biologic VMP multichannel potentiostat (BioLogic Science Instruments;

188 France). Both Ag/AgCl and Pt-wire were selected as reference and counter electrodes,

189 respectively. The three electrodes were immersed in a 0.1 M KOH water solution. As a working

190 electrode, a Rotating Disk Electrode (RDE) was used, i.e. Metrohm AUTOLAB RDE-2 with a

191 3 mm Glassy Carbon tip (Metrohm AG; Switzerland). The working electrode was prepared by

192 the deposition on the RDE tip of 10μl of a suspension containing 5 mg of the graphene-based

193 materials dispersed in 1 mL of a Nafion (5%) and water (1:9, v:v ratio) solution sonicated for

194 30 minutes.

195 CV experiments were carried out while bubbling N_2 or O_2 through the electrolyte solution

196 during the measurements with the potential interval of -0.8 to 0.4 V at a scan rate of 5 mVs^{-1}

197 and 50 mV s^{-1}. LSV curves were performed in a 0.1 M KOH solution saturated with O_2 at

198 different rotation speeds (i.e. 500, 1000, 1500, 2000, 2500, 3000 and 4000 rpm) with a scan

199 rate 5 mVs^{-1} and sweeping voltage ranged from 0.4 to -0.8 V. The experimental data were fitted

200 to the Koutecky-Levich model (Eqs. 4 and 5) in order to assess the electrocatalytic performance

201 of samples and to calculate the number of electrons transferred for each of them.

202 $$\frac{1}{J} = \frac{1}{J_k} + \frac{1}{B\omega^{0.5}} \qquad\qquad (4)$$

203 $$B = 0.2nF(D_{O_2})^{2/3}v^{-1/6}C_{O_2} \tag{5}$$

204 where j is the current density; J_k is the kinetic current density; ω correspond to the rotation

205 speed; F is the Faraday constant; v is the viscosity $(0.01\,\mathrm{cm^2\,s^{-1}})$ and D_{O2} and C_{O2} are the

206 oxygen diffusion coefficient $(1.9 \times 10^{-5}\,\mathrm{cm^2\,s^{-1}})$ and oxygen concentration

207 $(1.2 \times 10^{-6}\,\mathrm{mol\,cm^{-3}})$, respectively [38, 39].

208

209 *2.7. Adsorption kinetics and isotherms*

210 ACE adsorption kinetics were studied in order to stablish the time required to achieve the

211 adsorption equilibrium at saturation, reaching the equilibrium in 72 h (results not shown).

212 Adsorption isotherms of ACE from aqueous solutions were obtained by using 0.01 g of

213 prepared materials and 25 mL of pharmaceutical solutions at concentrations ranging from 10 to

214 100 mg L^{-1}.The suspensions were mechanically shaken until equilibrium was reached (72 h)

215 and measurements were performed at least twice to know their reproducibility. Equilibrium

216 concentrations were determined at 242 nm using a UV-spectrophotometer model UV-1800

217 Shimadzu. Adsorption isotherms were fitted to Langmuir and Freundlich equations (Eqs. 6 and

218 7, respectively):

219 $$\frac{C}{X} = \frac{1}{BX_m} + \frac{C}{X_m} \tag{6}$$

220 $$X = K_F \times C^{1/n} \tag{7}$$

221 where X is the amount adsorbed at a given equilibrium concentration, C, X_m is the adsorption

222 capacity, and B is the Langmuir constant. In the Freundlich equation C and X have the same

223 meaning, n (dimensionless) is an empirical parameter, and K_F is the so-called unit capacity

224 factor. So, K_F would be equivalent to the amount adsorbed at an equilibrium concentration of

225 1 mg L^{-1}.

226

227

228

229   *2.8.Electro-Fenton experiments*

230   The electro-Fenton (EF) experiments were carried out in an undivided glass cell with three

231   electrodes controlled by a Biologic VMP multichannel potentiostat (BioLogic Science

232   Instruments), containing 120 mL of ACE solution vigorously stirred with a magnetic bar. The

233   experiment setup of the device was as potenciostatic mode at -0.5V and -0.55V, based on the

234   ORR results. The reference electrode used was Ag/AgCl and the counter electrode was Pt-wire.

235   The working electrode (cathode) was prepared as previously reported by our group [40]. A

236   paste of 50 mg of graphene-based aerogels and polytetrafluoroethylene, PTFE (60% suspension

237   in water) was homogenous mixed with a ratio of 90:10. After that, the mixture was dried at

238   80°C overnight and the resulting material was homogeneously loaded on both sides of a

239   graphite sheet (50 mm x 8 mm). Solution of 10 mg L^{-1} of ACE and 0.5 M Na_2SO_4 as electrolyte

240   were used. The pH value of electrolyte was adjusted at 3.0 by H_2SO_4. Carbon-Fe_3O_4 (0.25 g L^{-1}

241   ^{1}) was added as catalysts. The O_2 gas was bubbled for 30 minutes before the experiment started

242   in order to saturate the solution and continuously bubbled during the experiment time. As

243   reference ACE removal without the addition of Fe_3O_4 or carbon- Fe_3O_4 was also conducted.

244   Samples for analysis were taken periodically from the glass cell, with immediate addition of a

245   proper amount of Na_2SO_3 for H_2O_2 reduction. The concentration of ACE was monitored using

246   a UV-spectrophotometer model UV-1800 Shimadzu at 242 nm. The concentration of dissolved

247   iron was analyzed colorimetrically by measuring the absorbance at 510 nm, according to ISO

248   6332:1988. The total organic carbon (TOC), determined with a TOC-VCSH Shimadzu

249   equipment, was used to evaluate the mineralization.

250

251   **3. Results and discussion**

252   *3.1. Characterization of the graphene-based materials and magnetic catalysts*

253 The porous texture of all the graphene-based materials and magnetic catalysts was studied by

254 N_2 adsorption-desorption and the results are given in Table 1. N_2 adsorption-desorption

255 isotherms for rGO-N-10 and rGO-N/S-10 and Fe_3O_4 and carbon-Fe_3O_4 catalysts are shown in

256 Fig. 1a-b, respectively. All isotherms of graphene-based materials can be described as type-II,

257 in accordance with IUPAC classification [41]. The progressive increase of the N_2 adsorbed

258 volume to higher relative pressures and the formation of a hysteresis loop of type H3 in both

259 samples, denotes a strong influence of mesoporosity on the isotherm profile.
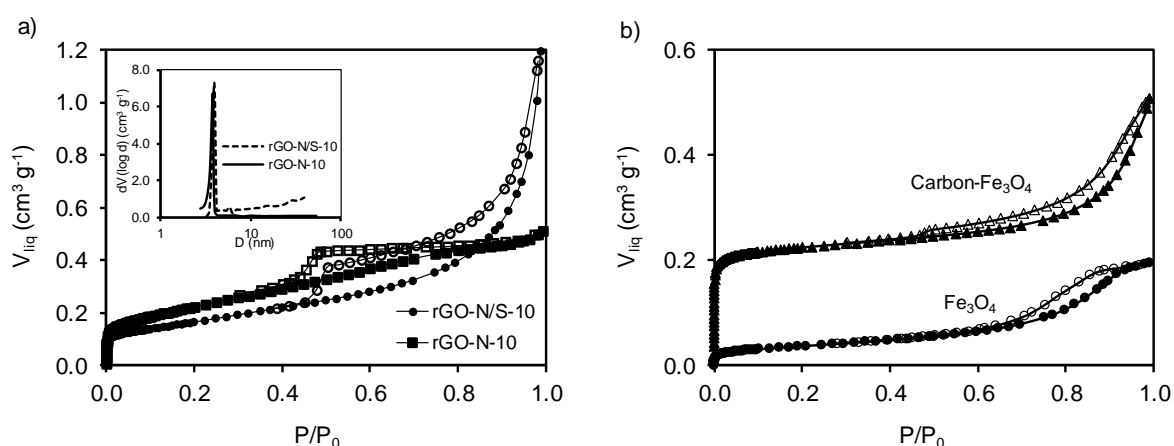
260

261 **Fig. 1.** a) Nitrogen adsorption-desorption isotherms and pore size distributions (inset; BJH

262 method) of rGO-N-10 and rGO-N/S-10; b) nitrogen adsorption-desorption isotherms of Fe_3O_4

263 and Carbon-Fe_3O_4.

264

265 The low surface area observed for GO (21 m^2 g^{-1}) seems to be related with the re-stacking of

266 the graphene sheets when the suspension is dried as previously observed [42]. It is shown that

267 a large increase in the S_{BET} and micropore and mesopore volume were observed for both N-

268 and N/S-doped samples in comparison with GO (Table 1). These results are likely due to the

269 partial exfoliation of GO during the preparation of the aerogels. It is noteworthy that the S_{BET},

270 micropore volume (W_0) of N-doped graphene aerogels were significantly higher than those

271 obtained for N/S- doped graphene aerogels (Table 1). These values increased with the content

272 of N, obtaining the highest S_{BET} and micropore volume for rGO-N-20 (592 m^2 g^{-1} and 0.229 cm^3

273   g^{-1}, respectively). Moreover, comparing the N_2 adsorption-desorption isotherms for both rGO-

274   N-10 and rGO-N/S-10 (Fig. 1a), a progressive increase of the N_2 adsorbed volume to higher

275   relative pressures (indicative of adsorption in wide micropores and mesopores) was observed.

276   On the other hand, mesopores volume of N/S-doped graphene aerogels were higher compared

277   to those in N-doped graphene aerogels (Table 1). The pore size distributions of N- and N/S-

278   doped graphene aerogels indicated mesopore diameter smaller than 6.0 nm. Such an improved

279   surface area and pore size distribution in the doped graphene aerogels could shorten the

280   diffusion path and provide more channels that may facilitate more efficiently the electrolyte

281   diffusion through the mesopores.

282

283   **Table 1.** Textural properties of the graphene-based materials and magnetic catalysts

284

Sample	S_{BET} $(m^2\,g^{-1})$	W_0 $(cm^3\,g^{-1})$	L_0 (nm)	V_{mes} $(cm^3\,g^{-1})$
rGO-N-5	583	0.228	1.44	0.26
rGO-N-10	489	0.191	1.51	0.28
rGO-N-20	592	0.229	1.41	0.30
rGO-N/S-5	441	0.178	1.35	0.55
rGO-N/S-10	374	0.143	1.46	0.55
rGO-N/S-20	432	0.164	1.46	0.57
GO	21	--	--	--
Fe_3O_4	78	--	--	0.18
Carbon-Fe_3O_4	551	0.216	0.68	0.18

293

294   Regarding magnetic catalysts (i.e. Fe_3O_4 and carbon-Fe_3O_4, Fig. 1b), the adsorption isotherms

295   belong to type IV with the H4 hysteresis loop. The specific surface area of the magnetic

296   catalysts increased with the presence of carbon gel (i.e. 78 to 551 $m^2\,g^{-1}$ for Fe_3O_4 and carbon-

297   Fe_3O_4, respectively. Moreover, the results show that carbon-Fe_3O_4 presents an important micro

and mesopores network pore volumes: 0.216 and 0.18 cm^3 g^{-1}, respectively and a micropore

width (L_0) of 0.68 nm.

Table 2 listed the results of the elemental analysis of the graphene-based materials showing the

larger percentage of oxygen content for GO (i.e. 53.5%). It is interesting to note that mostly of

oxygenated groups were removed during the thermal treatment and doping of the materials

showing a N or N/S incorporation (depending of the precursor, i.e. urea or thiourea,

respectively) at the same time.

Table 2. Elemental analysis (% wt.) and intensity ratios of the D bands relative to the G mode
for the graphene-based materials.

| Sample	N	C	H	S	O	I_D/I_G
	%	%	%	%	%	532 nm
rGO-N-5	7.1	69.3	3.1	0.0	20.5	1.11
rGO-N-10	8.2	70.7	3.0	0.0	18.1	1.08
rGO-N-20	9.3	70.2	2.8	0.0	17.7	1.09
rGO-N/S-5	1.7	71.3	3.0	1.1	22.9	1.13
rGO-N/S-10	1.8	72.1	3.4	1.3	21.4	1.16
rGO-N/S-20	2.1	72.8	3.7	1.4	20.2	1.12
rGO	0.0	71.5	5.2	0.1	23.2	1.07
GO	0.1	42.6	3.6	0.2	53.5	0.85

In general, as the ratio of GO:urea or GO:thiourea increased, the N and S content in the samples

also increased (Table 2). In particular, 9.3% of N was determined for rGO-N-20 whereas the

material prepared with the highest ratio GO:thiourea, (i.e. 1:20 in rGO-N/S-20) showed values

of 2.1% and 1.4% of N and S, respectively. It seems that N-doping was more effective than N/S

doping, in agreement with previous publications [43, 44].

TEM and SEM analysis were performed for the visualization of the morphology of the prepared

materials. TEM micrograph of the GO is shown in Fig. 2a, indicating the presence of graphene

316   multilayers. Typical SEM micrographs of rGO-N-10 (Fig. 2b), Fe_3O_4 (Fig. 2c) and carbon-

317   Fe_3O_4 (Fig. 2d) clearly reveal the differences in the morphology of the materials. rGO-N-10

318   exhibit 3D interconnected structure of aggregated wrinkled graphene layers. SEM image of

319   Fe_3O_4 (Fig. 2c) indicated clusters of spherical-like particles whereas the micrograph of carbon-

320   Fe_3O_4 showed a more compact structure which can be explained by the introduction of

321   magnetite in the crystalline space of the gel (Fig. 2d).
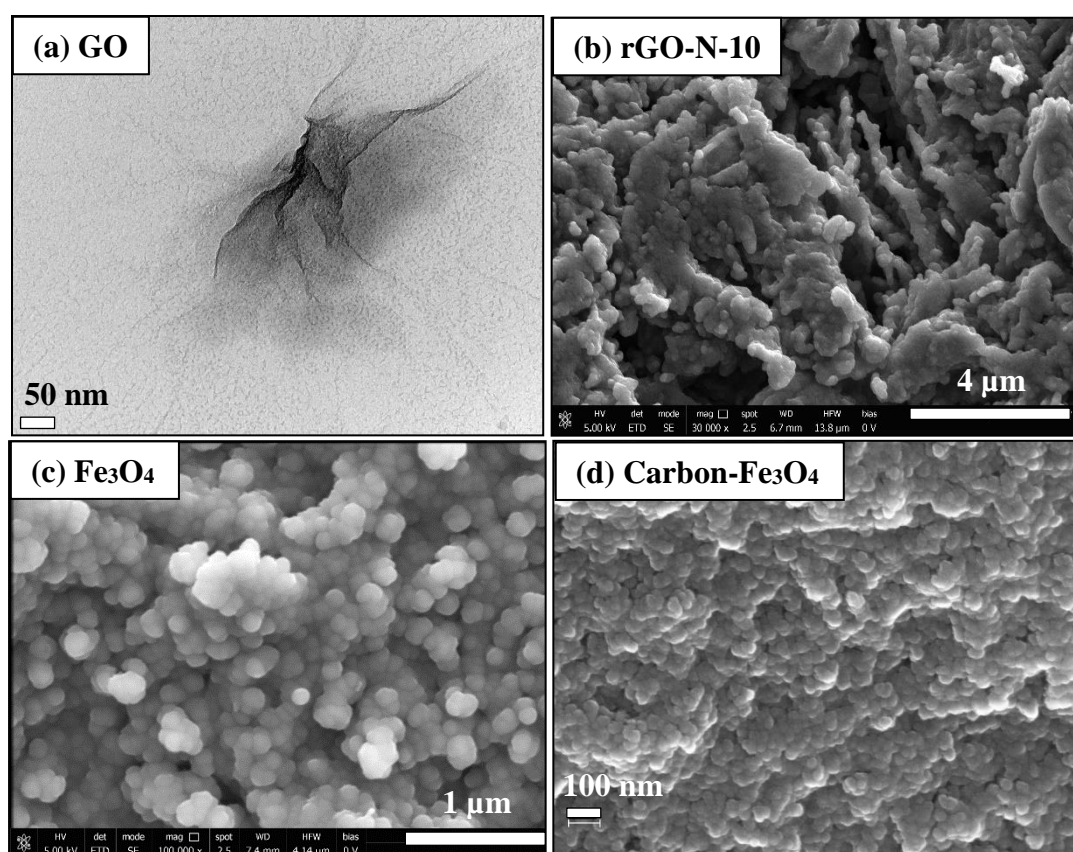
Fig. 2. a) TEM micrograph of GO and SEM micrographs of b) rGO-N-10; c) Fe_3O_4 and d) Carbon-Fe_3O_4.

338   Raman spectra are shown in Fig. 3. All samples exhibited the graphitic G band at ~1582 cm^{-1},

339   D band ~1345 cm^{-1} and the high frequency modes, including the 2D band (~2700 cm^{-1}) that

340   result of an overtone of the D band, as well a D+G peak which is result of a combination of D

341   and G peaks and appears over 2950 cm^{-1} [45]. The graphitic G band corresponds to the

stretching vibration mode of sp^2 carbon atoms [46, 47], the D-band reflect the disorder-induced character in the aromatic rings whereas its overtone (2D-band) give information in sp^3 generated defects (D-band) and exfoliation of individual graphene sheets (2D band) that lead to electronic decoupling [48]. Defects in graphitic plane are important due to the high anisotropy in the mechanical strength and the in/out plane electrical conductivity in order to improve the performance of carbon based materials in different applications [49].
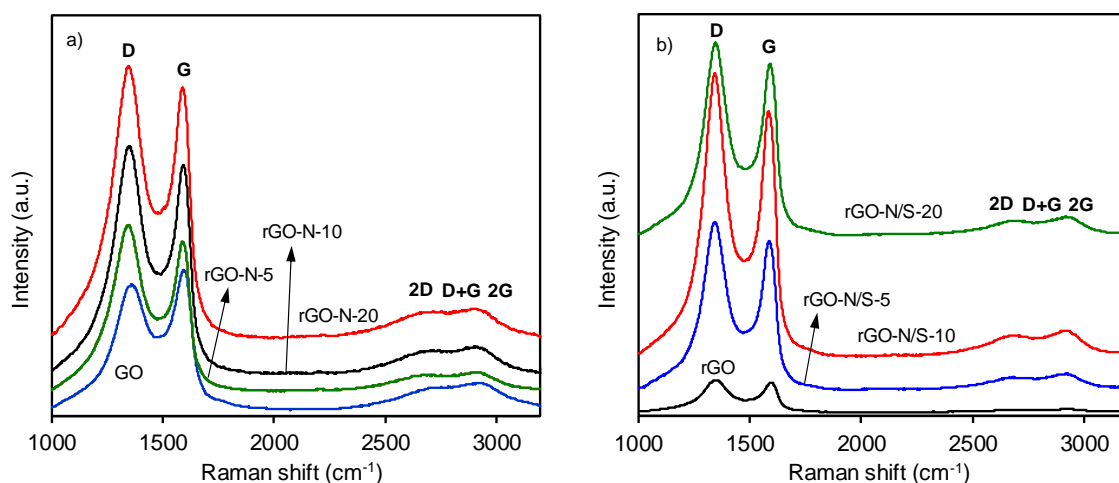
Fig. 3. Raman spectra of a) GO and N doped graphene materials and b) rGO and N/S doped graphene materials.

Table 2 listed the Raman intensity ratios of the D bands relative to the G mode (I_D/I_G) obtained for the graphene-based materials, calculated from the areas of the corresponding Raman bands, at 532 nm. The I_D/I_G ratio is a degree representation of defects and disorder levels of structural ordered carbon in the graphitic materials [50]. As seen in Table 2, the I_D/I_G ratio was larger for rGO and for the heteroatom doped graphene materials comparing to GO. This change can be attributed to a decrease in the average size of the sp^2 domains upon removal of oxygen groups from GO during the doping process, suggesting the presence of abundant defects in the materials [51]. In particular, both rGO-N-10 and rGO-N-20 presented the lowest I_D/I_G values (i.e. 1.08 and 1.09, respectively) suggesting that these materials contain the lowest amount of defects.

362
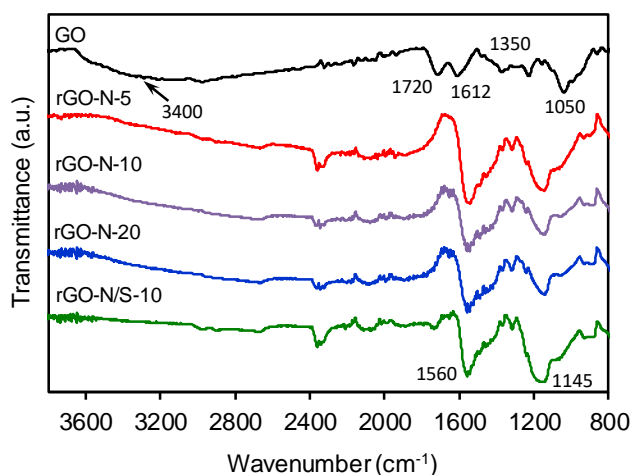
Fig. 4. FTIR-ATR spectra of GO, rGO-N-5, rGO-N-10, rGO-N-20 and rGO-N/S-10.

363
364

365 FTIR-ATR were studied for all the materials. In particular, the spectra of GO, rGO-N-5, rGO-

366 N-10, rGO-N-20 and rGO-N/S-10 are depicted in Fig. 4. GO showed a broad band situated ca.

367 3400 cm^{-1}, assigned to the vibration of C-OH groups, a band at ca. 1720 cm^{-1} attributed to

368 carbonyl groups, C=O, and a band at ca. 1350 cm^{-1} corresponds to C-OH stretching. The band

369 at ca. 1220 cm^{-1} corresponds to breathing vibrations of epoxy groups (-O-) and the band at ca.

370 1050 cm^{-1} is attributed to the stretching vibration of C-O groups. The band at ca. 1612 cm^{-1} can

371 be assigned to the skeletal vibration of graphene sheets. Compared to that of GO, the peak

372 intensities of the oxygen functional groups for the heteroatom graphene-based materials

373 become very weak indicating the partial removal of the oxygen-containing groups during the

374 doping process [42]. For rGO-N-5, rGO-N-10, rGO-N-20 and rGO-N/S-10 materials, a band

375 likely corresponding to sp^2 aromatic C=C and C=N bonds [52] was observed at ca. 1560 cm^{-1}.

376 Moreover, the rGO-N/S-10 showed a more prominent peak at around 1100-1145 cm^{-1} which

377 most probably corresponds to the peak of the C-S-C bond symmetrical stretching vibration [53],

378 but also possible to the other bonds of C-O-C, that explain the peak in the samples without

379 sulphur doping such as rGO-N-5, rGO-N-10 and rGO-N-20.

380

381

382
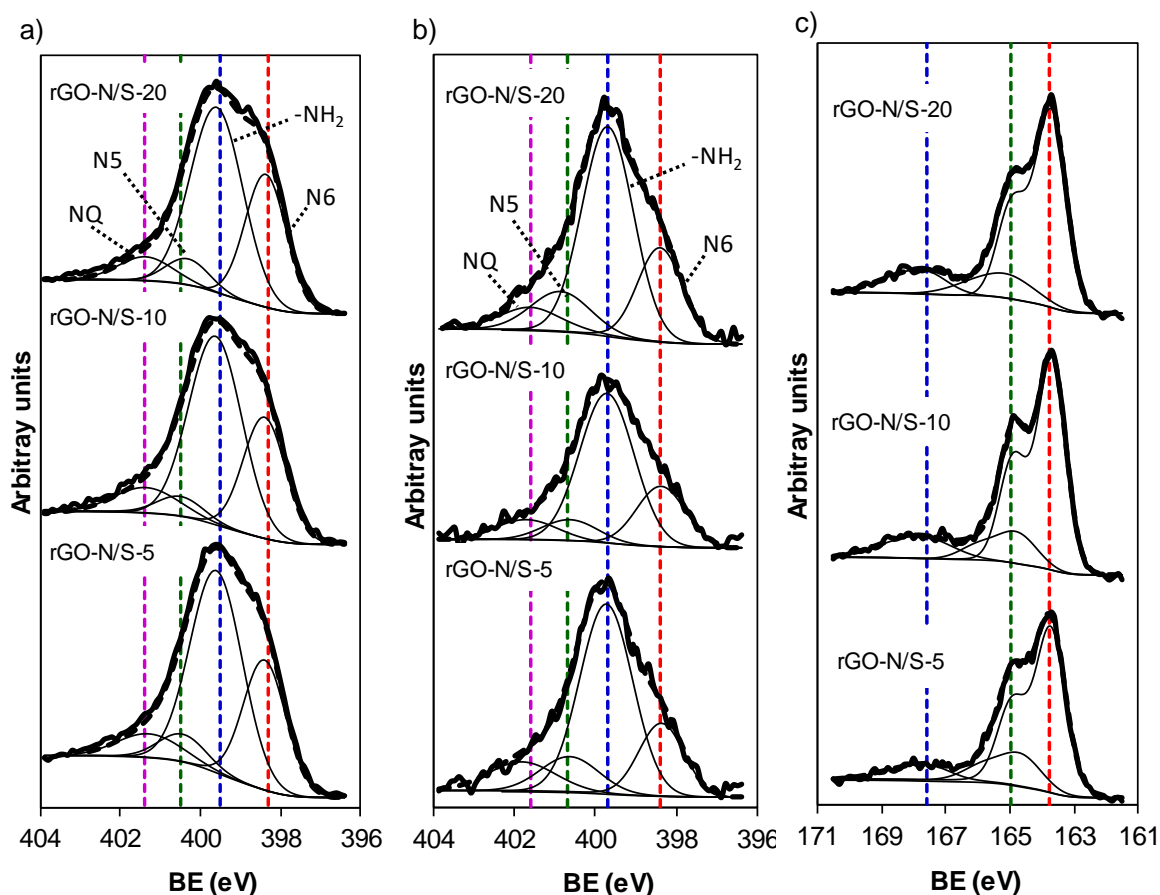
To further investigate the nitrogen and sulphur content on the heteroatom graphene samples, X-ray photoelectron spectroscopy (XPS) signals were analyzed as illustrated in Fig. 5. XPS data for nitrogen, sulphur and oxygen contents are collected in Table 3. Fig. 5a shows the deconvoluted N1s XPS spectra for rGO-N-5, rGO-N-10 and rGO-N-20, revealing the presence of four types of species, namely graphitic N (or quaternary N, NQ), pyrrolic N (N5), amino groups (-NH$_2$) and pyridinic N (N6) at ~401.3, ~400.4, ~399.6 and ~398.4 eV, respectively, consistent with the results for other N-doped carbon materials [54, 55]. It is interesting to mention that he most abundant N specie in the N-doped graphene materials correspond to the amino groups (-NH$_2$), followed by the N-pyridinic species (N6) and finally both N-pyrrolic form (N5) and N-graphitic (NQ) with the lowest amount as previously observed [42]. It can be

17

generally accepted that the covalent functionalization with amino groups can occur at the edge or defect sites of GO, where are more chemically active than those within the plane of graphene [56].

Table 3. Nitrogen and sulphur species percentage and corresponding binding energies (in brackets, eV) and nitrogen, sulphur and oxygen content (% wt.) obtained by XPS analysis.

Sample	N (%)	S (%)	O (%)	N Peak (%)				S Peak (%)		
				(N6)	(-NH$_2$)	(N5)	(NQ)	C-S-C	R$_2$-S=O	C–SO$_x$–C
rGO-N-5	7.6	--	11.6	29 (398.4)	56 (399.6)	7 (400.4)	8 (401.3)	-	-	-
rGO-N-10	7.6	--	12.8	29 (398.4)	57 (399.6)	5 (400.5)	9 (401.4)	-	-	-
rGO-N-20	7.8	--	11.0	31 (398.4)	55 (399.6)	7 (400.3)	8 (401.4)	-	-	-
rGO-N/S-5	1.8	2.0	17.0	19 (398.4)	58 (399.8)	12 (400.7)	11 (401.8)	73 (163.7)	18 (164.6)	9 (167.5)
rGO-N/S-10	1.5	2.1	15.7	22 (398.4)	60 (399.7)	9 (400.7)	10 (401.7)	73 (163.7)	14 (164.7)	13 (167.6)
rGO-N/S-20	1.9	1.9	15.9	22 (398.4)	57 (399.7)	13 (400.9)	8 (401.6)	43 (163.7)	14 (165.0)	12 (167.6)

The N/S doped graphene materials, N1s and S2p XPS deconvoluted spectra are shown in Figs. 5b and c, respectively. The N1s XPS spectra for rGO-N/S-5, rGO-N/S-10 and rGO-N/S-20 showed also the presence of pyridinic-N, amino, pyrrolic-N and graphitic-N functionalities (Table 3). Regarding the deconvoluted S2p XPS spectra, each S2p peak is the resultant of two components ($2p_{1/2}$ and $2p_{3/2}$) although only the sum of both peaks was plotted in Fig. 5c, being $2p_{3/2}$ binding energy the one used to assign different peaks to chemical functionalities. Considering that, the deconvoluted S2p XPS spectra showed three different chemically shifted components, which are attributed to the S-thiophene-like groups (C-S-C) at ~163.7 eV, sulphoxide groups (R$_2$-S=O) at ~164.6 eV and a low intense component associated with

412 oxidized forms of sulphur, i.e. sulphone groups (C–SO_x–C) at ~167.5 eV, as previously reported

413 [57, 58]. Once again, the predominant nitrogen specie in the N/S- doped-graphene materials

414 was the amino group (-NH_2), whereas the most abundant sulphur-containing functionalities

415 correspond to the S-thiophene (Table 3) consistent with previous results in literature for

416 graphene-doped materials [42].

417 The XRD patterns of the Fe_3O_4 and carbon-Fe_3O_4 catalysts are shown in Fig. 6. The peaks

418 indexed as lattice planes (111), (220), (311), (400), (422), (511) and (440) confirm the

419 formation of Fe_3O_4 crystal with a cubic spinel structure (JCPDS card no. 85-1436) [59]. The

420 broader peak shown in the XRD pattern in the range of 20-30° of the carbon-Fe_3O_4 composite

421 material can be related to the lower dimensions of the crystallites and may also suggest the

422 presence of amorphous material.
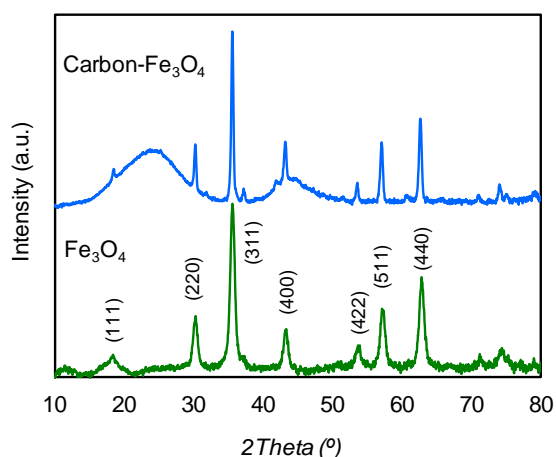
423

424 **Fig. 6.** XRD patterns of Fe_3O_4 and carbon-Fe_3O_4 catalysts.

425

426 *3.2.Oxygen reduction reaction: CV and LSV*

427 The electrocatalytic ORR activity of the GO and N- and N/S-doped graphene aerogels was

428 firstly assessed by cyclic voltammetry (CV). Fig. S1a-e (supplementary information) depict the

429 electrochemical responses of GO, rGO-N-5, rGO-N-10, rGO-N-20, rGO-N/S-5, rGO-N/S-10

430 and rGO-N/S-20 respectively, under an O_2- or N_2- saturated KOH solution (0.1 M) recorder at

431 a scan of 50 mV s^{-1} and using a RDE rotation speed of 1000 rpm. The results showed a

significant reduction process under O_2 indicating that all the prepared graphene-based materials were electroactive to the O_2 reduction. Moreover, no cathodic peak for ORR was shown in N_2-saturated electrolyte. In general, the presence of heteroatoms (Fig. S1 b-e) increased the capacitance significantly in comparison to that obtained for the undoped material (Fig. S1a).
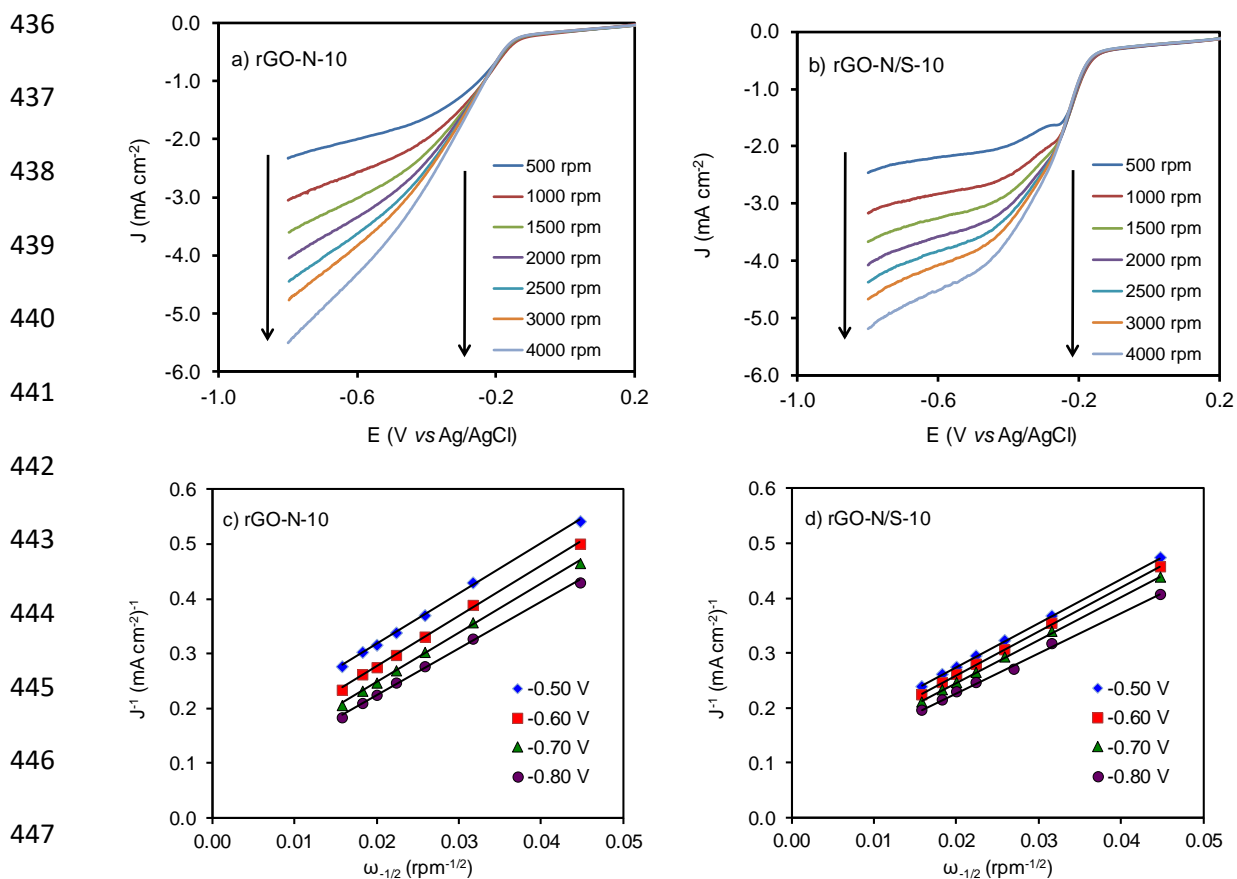
Fig. 7. a-b) LSV at different rotation speed and c-d) K-L plots at different electrochemical potentials from -0.5V to -0.8V for rGO-N-10 (a and c) and rGO-N/S-10 (b and d).

Among all the heteroatom-doped graphene materials, both rGO-N-5 and rGO-N-20 showed the lower ORR activity (Figs. S1b and S1d, respectively) whereas all the samples treated with thiourea (i.e. rGO-N/S-5, rGO-N/S-10 and rGO-N/S-20) exhibited a great performance for ORR. These results demonstrate the synergistic effect caused by N and S co-doping increasing the electron density on the surface of the carbon material and promoting the oxygen reduction reactions as previously reported [22, 60, 61]. These results show that capacitance in carbon

458 materials could be also related to the porous texture. Thus, N/S-doped graphene materials

459 presented the highest mesopore volume in comparison with the N-doped materials (V_{mes}, Table

460 1) which are of great importance for the rapid mass transport in electrocatalytic processes [62].

461
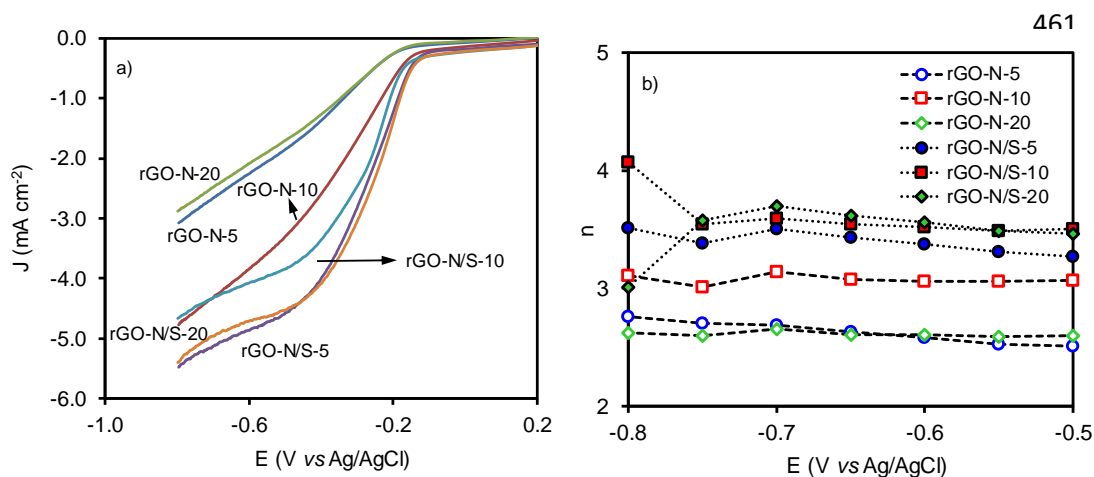
467 **Fig. 8**. a) LSV curves at 3000 rpm and b) variation of n with E *vs* Ag/AgCl for heteroatom
468 graphene-based materials.

469

470 LSV measurements at a different rotating speed were also used to examine the ORR activity of

471 the samples. In particular, Figs. 7a and b depicts the LSV curves for both rGO-N-10 and rGO-

472 N/S-10, at rotating speeds from 500 to 4000 rpm and in O_2-saturated 0.1 M KOH electrolyte. It

473 can be seen that the limit current density increases with the increase of rotating speed

474 correspondingly. In order to obtain the number of electrons transferred at each potential and

475 evaluate the type of the ORR mechanism (i.e. 4 or 2-electrons), the LSV curves at different

476 rotation speeds were adjusted to Koutecky-Levich equation (Figs. 7c and d for rGO-N-10 and

477 rGO-N/S-10, respectively). The corresponding K-L plots exhibit a good parallel linear

478 relationship from -0.50 to -0.80 V, suggesting the consistent electron transfer number of the

479 ORR at different electrode potentials. LSV curves at a rotation speed of 3000 rpm for all the

480 heteroatom doped materials are shown in Fig. 8a. The parameters determined from the analysis

481 of LSV curves (values of J_k and n refer to K-L fitting for data at -0.80, -0.50 and -0.55V) are

482 listed in Table 4. Fig. 8b depicted the variation of the number of electrons transferred with the

electrochemical potential for each sample. The results showed that both samples rGO-N/S-5

and rGO-N/S-20 exhibited the better performance toward ORR with the higher values of current

density (respectively, 20.933 and 17.298 mA cm^{-2} at -0.80 V, Table 4).

It is observed that the electron transfer number of the rGO-N/S-10 material is calculated to be

ca. 4.0 at -0.8V, indicating that this material catalysed ORR mainly through a four-electrons

pathway resulting a negligible hydrogen peroxide intermediate generated. Moreover, among

the N/S-heteroatom graphene samples, ORR starts at lower potential using both rGO-N/S-10

and rGO-N/S-20 (i.e. 0.834 and 0.810V, respectively, E$^0_{onset}$ versus Ag/AgCl). The improved

ORR activity of N/S-doped graphene materials in comparison with N-doped graphene materials

can be ascribed to the enhanced synergetic effect between N and S dopants which can alter the

electronic structure of the sp^2 carbon atoms as previously reported as well as the favourable

texture contribution from the mesopores volume [22, 61].

Table 4. Parameters obtained from the analysis of LSV curves for data at -0.8, -0.55 and -0.5
V.

Sample	E$^0_{onset}$ (-0.80) (V)	J_k (-0.80) (mA cm^{-2})	n (-0.80)	J_k (-0.55) (mA cm^{-2})	n (-0.55)	J_k (-0.50) (mA cm^{-2})	n (-0.50)
rGO-N-5	-0.206 (0.771) [*]	6.808	2.76	3.487	2.52	2.943	2.50
rGO-N-10	-0.162 (0.815) [*]	18.324	3.11	6.068	3.05	7.455	3.07
rGO-N-20	-0.178 (0.799) [*]	6.245	2.62	3.044	2.59	2.583	2.60
rGO-N/S-5	-0.180 (0.797) [*]	20.933	3.52	17.319	3.31	15.870	3.27
rGO-N/S-10	-0.143 (0.834) [*]	13.055	4.05	9.600	3.48	8.870	3.50
rGO-N/S-20	-0.167 (0.810) [*]	17.298	3.00	14.292	3.49	13.500	3.47
rGO	--	--	--	1.02	1.08	1.10	1.15
GO	--	--	--	0.320	2.45	0.272	3.70

[*]In parentheses, potentials versus the reference hydrogen electrode (RHE) obtained from the conversion of the
measured potentials versus Ag/AgCl reference electrode using the Nernst equation.

501   On the other hand, rGO-N-5 and rGO-N-20 exhibited electron transfer number ranges from

502   2.76 to 2.50 and 2.62 to 2.60, respectively, depending on the potential (Table 3). It is well

503   known that the nitrogen content had a significant effect on ORR catalytic activity. Both

504   pyridinic N and graphite N seems to be the main active sites to produce H_2O_2 in 2e$^-$ pathway

505   following Eq. (8), as previously reported [18].

506     $O_2 + H_2O + 2e^- \rightarrow HO_2^- + HO^-$ (8)

507   In general, ORR performance of heteroatom-doped carbon materials is mainly determined by

508   (i) the chemical composition and bonding configurations of the doped atoms and (ii) the specific

509   surface area and porous texture. In our case, N/S-doped graphene materials showed better

510   performance for ORR leading a 4 e$^-$ pathway and also a high current density. On the other hand,

511   the introduction of N functionalities in graphene materials favoured the 2e$^-$ ORR process with

512   the subsequence H_2O_2 generation. The better catalytic performance of N/S- doped materials

513   might be ascribed to the role of N/S doping which form C-N and C-S bonds (Fig. 5) and could

514   alter the electronic structure of the sp^2 carbon atoms as previously reported [63]. Indeed,

515   positively charged carbon atoms can be generated, due to the electron-accepting nature of

516   nitrogen atoms with respect to carbon atoms. These atoms can act as active sites to adsorb O_2

517   molecules and weaken O-O bonds [22]. Regarding S dopant, the role of S could be related to

518   the mismatch of the farthermost orbitals between sulphur and carbon, resulting in the generation

519   of positive charge on the sulphur atoms, which can act as electrocatalytic centers for ORR.

520   Apart from the role of electronic structure, the best ORR performance of N/S-doped graphene

521   materials could be also ascribed to the higher mesoporous structure of these materials compared

522   to N-doped graphene samples (Table 1) which can facilitate the transport of both oxygen and

523   electrolyte, lowering the resistance of mass transport [62].

524   The obtained results indicated that the highest electrogeneration of H_2O_2 at cathode by ORR

525   can be found for both rGO-N-5 and rGO-N-20 catalysts. For this reason, these materials were

526   selected for the subsequent electro-Fenton (EF) experiments. Moreover, a material with mainly

527 4 e⁻ pathway (i.e. rGO-N/S-10) was also studied in the EF experiments in order to compare the

528 results with that of both rGO-N-5 and rGO-N-20 samples.

529

530   *3.3. Adsorption equilibrium studies*

531 Preliminary experiments were performed to establish the adsorption-desorption equilibrium of

532 ACE at room temperature on the selected materials for EF process, i.e. rGO-N-5, rGO-N-20

533 and rGO-N/S-10. Fig. S2 (supplementary information) depicts adsorption isotherms of ACE

534 from distilled water at 298 K on rGO-N-5, rGO-N-20 and rGO-N/S-10 materials. Adsorption

535 isotherms were fitted to Langmuir and Freundlich equations and the results obtained are listed

536 in Table S1 (supplementary information). In general, the linear regression coefficient values

537 show that the Langmuir equation fitted better the adsorption isotherms than the Freundlich one

538 (Table S1). Langmuir equation enables to know the adsorption capacity of the adsorbents and

539 the B constant from which the adsorption thermodynamic parameters can be obtained. The

540 maximum adsorption capacity (X_m) was 116, 120 and 88 mg g^{-1} for rGO-N-5, rGO-N-20 and

541 rGO-N/S-10, respectively. These results are in accordance with the textural characteristics of

542 the materials obtained, thus, both rGO-N-5, rGO-N-20 catalysts exhibited higher values of

543 surface area and micropore volume (i.e. S_{BET} of 583 and 592 m^2 g^{-1} and W_0 of 0.228 and 0.229

544 cm^3 g^{-1}, respectively) in comparison with that obtained for rGO-N/S-10 (374 m^2 g^{-1} and 0.143

545 cm^3 g^{-1}, respectively). Regarding the B constant, the highest value obtained for rGO-N-20 (i.e.

546 0.23 L mg^{-1}) seems to be related with the strongest adsorbent-adsorbate interactions on the rGO-

547 N-20 sample.

548

549   *3.4. Electro-Fenton*

550 The electro-Fenton (EF) experiments were carried out using the saturated selected heteroatom

551 graphene-based materials, i.e. rGO-N-5, rGO-N-20 and rGO-N/S-10. These catalysts were

552 tested in the degradation of 10 mg L^{-1} of ACE by EF process at -0.55 V for 360 min. The

553 experiments were performed using carbon-Fe_3O_4 as catalysts to activate the generated H_2O_2 for

554 the degradation of the contaminant (Fig. 9). A blank experiment for the rGO-N-5 sample was

555 investigated in order to quantify the amount of ACE degraded in the absence of magnetic

556 samples. Table 5 summarizes the TOC conversion, ACE conversion and leaching of iron

557 species at the end of the experiments.

558 It well known that the current density is responsible for the reduction of oxygen resulting the

559 formation of hydrogen peroxide at the cathode. Thus, it was observed that for current intensity

560 values under 3.0 mA cm^{-2}, obtained with potential below -0.5 V (Table 4), a negligible ACE

561 degradation was achieved (results not shown). These results seem to be related with the

562 inefficient oxygen reduction due to the lower energy supplied to the system as previously

563 reported [28]. For the EF experiments, potential value of -0.55 V was selected for the EF

564 reaction, according to the obtained values of J_k, n (Table 4) and the respective ACE degradation

565 (Table 5). For the materials in which the electron transfer number is ca. 2 at -0.55V (i.e. 2.52

566 and 2.59 for rGO-N-5 and rGO-N-20, respectively) and using carbon-Fe_3O_4 as catalyst, the EF

567 results showed that rGO-N-5 promote the highest ACE conversion, reaching almost complete

568 removal in 240 min whereas rGO-N-20 exhibited a 71% of ACE conversion (Table 2).

569 However, a different tendency was observed for the ACE mineralization; i.e. after 360 min;

570 rGO-N-5 (+ Carbon-Fe_3O_4) produced a TOC reduction of 45.5% while rGO-N-20 leads to a

571 TOC reduction of 51.6% (Table 5). These results could to be related with the the larger amount

572 of iron leached obtained for rGO-N-20 compared to that obtained for rGO-N-5 (respectively

573 0.33 and 0.24 mgL^{-1}). On the other hand, and as expected, rGO-N/S-10 showed the lowest

574 performance (23 and 13.1% of ACE conversion and mineralization, respectively) due to the

575 mainly 4-electron pathway for ORR that implies a much lower generation of H_2O_2 (Table 4) in

576 comparison with that obtained for rGO-N-5 or rGO-N-20 samples.
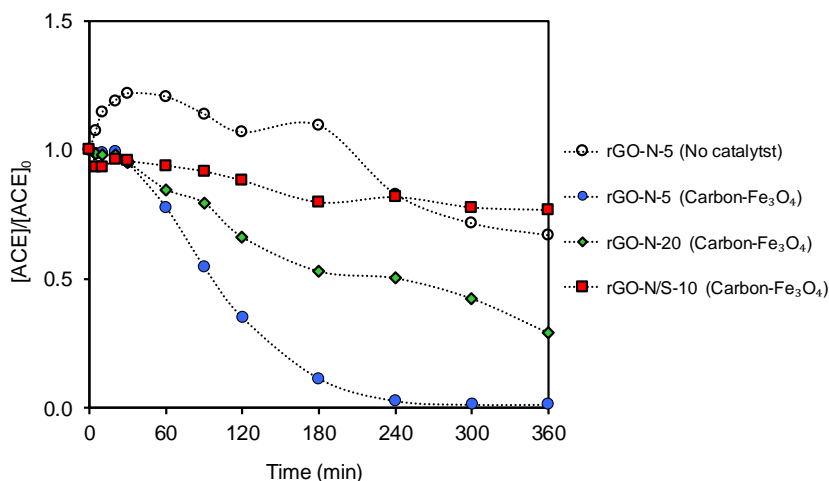
Fig. 9. Normalized ACE concentration ($[ACE]/[ACE]_0$) as function of time for electro-Fenton experiments performed with the saturated samples rGO-N-5, rGO-N-20 and rGO-N/S-10 and using carbon-Fe_3O_4 as catalyst at potential of -0.55V. A non-catalytic blank experiment for rGO-N-5 without catalyst is also shown for comparison.

The influence of pH on the EF degradation of ACE at natural solution pH (i.e. 5.7) is shown in Fig. S4 (supplementary information). As expected, the efficiency of the EF process decreases at higher initial solution pH. This can be explained by the precipitation of iron species as ferric hydroxides as well as the decomposition of generated H_2O_2 into water and O_2, thus hindering the production of $HO^\bullet$, as previously reported [31]. Nevertheless, it is of special interest to note that ACE degradation of approximately 70% was obtained using rGO-N-5 at neutral reaction pH (Fig. S4). More studies will be further required to improve the catalyst stability at natural solution pH.

A blank experiment was also investigated in order to quantify the amount of ACE degraded under non-catalytic conditions (rGO-N-5 no catalyst). The results showed that although a desorption of ACE was occurring during the first 180 minutes, an ACE conversion of 33% with a TOC reduction of 5.0% was achieved at the end of the experiments, i.e. 360 min (Table 5). These results could be due to the formation of $HO^\bullet$ radicals in the absence of catalyst. In fact, it has been reported that the presence of N-functionalities (such as pyridinic N and graphitic)

597   could catalyze H_2O_2 to the production of radicals $HO^{\bullet}$ [18]. However, the catalysis of H_2O_2 to

598     $HO^{\bullet}$ was much slower than that of H_2O_2 generation, which lead to the accumulation of H_2O_2.

599   For that reason, the use of an active catalyst, i.e. carbon-magnetite is crucial to accelerate the

600   generation of radicals, favoring the conversion and degradation of ACE (Table 5).

601   Heteroatom graphene-based materials could promote the $2e^-$ ORR process to electrochemically

602   generate H_2O_2 and the presence of carbon-Fe_3O_4 could efficiently catalyze H_2O_2 to produce

603     $HO^{\bullet}$ radical for ACE degradation. In literature, the reaction mechanism seems to be mostly

604   motivated by $HO^{\bullet}$ radicals attack during the EF process, although the formation of other reactive

605   species such as radical superoxide anion $(O_2^{\bullet-})$ can assume a representative role in the EF

606   mechanism [18] following Eq. (9). After the generation of radicals, ACE might be attacked and

607   degraded into different aromatic by-products such as benzoic acid, benzaldehyde and

608   acetamide, among others, as well as aliphatic organic acids such as fumaric, oxalic, acetic,

609   formic and maleic acids, as previously reported [64]. Even so, more studies will be further

610   required, perhaps using more advanced characterization techniques for exact identification of

611   all reaction intermediates of ACE.

612     $O_2 + e^- \rightarrow O_2^{\bullet-}$ (9)

613   On the other hand, post-reaction analysis of the rGO-N-5 and rGO-N-20 (EF) samples by XPS

614   (results not shown) indicated that nitrogen functionalities were stable and there are not

615   significant changes of the N groups after ACE oxidation by EF.

616

617   **Table 5**. ACE conversion ($X_{ACE,360min}$), total organic carbon conversion ($X_{TOC,360min}$) and

618   leaching of iron species ($C_{Fe-leached}$) in EF experiments at -0.55V after 360 min.

Sample	$X_{ACE,360min}$ (%)	$X_{TOC,360min}$ (%)	$C_{Fe-leached}$ (mg L^{-1})
Blank (rGO-N-5 no catalyst)	33	5.0	--
rGO-N-5 (+carbon-Fe_3O_4)	100	45.5	0.24
rGO-N-20 (+carbon-Fe_3O_4)	71	51.6	0.33
rGO-N/S-10 (+carbon-Fe_3O_4)	23	13.1	0.15

619

Regarding the Fe leached at 360min (Table 5), it is noteworthy that all the catalysts tested

present values much lower than the maximum dissolved iron concentration allowed in

European Union standards for discharge of treated waters (i.e. 2.0 mg L^{-1}). The concentration

of leaching of iron species was 0.24, 0.33 and 0.15 mg L^{-1} for rGO-N-5 (+carbon-Fe_3O_4), rGO-

N-20 (+carbon-Fe_3O_4) and rGO-N/S-10 (+carbon-Fe_3O_4), respectively. The lower amount of

iron leached obtained for all the samples indicate that the Fenton reaction is taking place

heterogeneously between iron supported on carbon and the generated H_2O_2 in solution,

confirming the higher stability of the catalysts. Besides the high stability of the carbon catalyst,

they have an additional advantage of the magnetically recoverable catalysts.

4. Conclusions

A series of N- and N/S-doped graphene aerogels were prepared by simple hydrothermal method

and freezing-drying process using urea or thiourea as N or N/S source, respectively.

Electrochemical characterization was carried out to assess the electro-catalytic performance and

the number of electrons transferred of each sample for ORR. The N-functionalities introduced

in the graphene-based material remarkably influence the catalytic performance in both

processes. In general, N/S-doped graphene aerogels show better performance for ORR leading

a four- electron pathway and also high current densities. The improved catalytic performance

can be attributed to the enhanced synergetic effect between N and S dopants. The introduction

of N functionalities in GO favour the $2e^-$ ORR process for H_2O_2 generation. Heterogeneous

electro-Fenton process for the degradation of acetaminophen using both N-graphene aerogels

and magnetically recoverable catalyst based on carbon-magnetite, allowed a contaminant

removal of ca. 100%, ca. 45% of mineralization and also a low iron loss by leaching (ca. 0.24

644 mg L^{-1}), conforming with the European Union directives for discharge of treated waters. The

645 selected magnetic carbon catalyst also exhibits good stability.

646
647

655

656 **References**

657 [1] P. Paíga, L.H.M.L.M. Santos, C. Delerue-Matos, Development of a multi-residue method

658 for the determination of human and veterinary pharmaceuticals and some of their metabolites

659 in aqueous environmental matrices by SPE-UHPLC–MS/MS, Journal of Pharmaceutical and

660 Biomedical Analysis, 135 (2017) 75-86.

661 [2] S. Comber, M. Gardner, P. Sörme, D. Leverett, B. Ellor, Active pharmaceutical ingredients

662 entering the aquatic environment from wastewater treatment works: A cause for concern?,

663 Science of The Total Environment, 613-614 (2018) 538-547.

664 [3] C.G. Daughton, Pharmaceuticals and the Environment (PiE): Evolution and impact of the

665 published literature revealed by bibliometric analysis, Science of The Total Environment, 562

666 (2016) 391-426.

667 [4] F. Desbiolles, L. Malleret, C. Tiliacos, P. Wong-Wah-Chung, I. Laffont-Schwob,

668 Occurrence and ecotoxicological assessment of pharmaceuticals: Is there a risk for the

669 Mediterranean aquatic environment?, Science of The Total Environment, 639 (2018) 1334-

670 1348.

671 [5] L.H.M.L.M. Santos, A.N. Araújo, A. Fachini, A. Pena, C. Delerue-Matos, M.C.B.S.M.

672 Montenegro, Ecotoxicological aspects related to the presence of pharmaceuticals in the aquatic

673 environment, Journal of Hazardous Materials, 175 (2010) 45-95.

674 [6] C. Miège, J.M. Choubert, L. Ribeiro, M. Eusèbe, M. Coquery, Fate of pharmaceuticals and

675 personal care products in wastewater treatment plants – Conception of a database and first

676 results, Environmental Pollution, 157 (2009) 1721-1726.

677 [7] K. Fent, A. Weston, D. Caminada, Ecotoxicology of human pharmaceuticals, Aquatic

678 Toxicology, 76 (2006) 122-159.

679 [8] S. Ahmadzadeh, M. Dolatabadi, Removal of acetaminophen from hospital wastewater using

680 electro-Fenton process, Environmental Earth Sciences, 77 (2018).

681 [9] H. Olvera-Vargas, J.-C. Rouch, C. Coetsier, M. Cretin, C. Causserand, Dynamic cross-flow

682 electro-Fenton process coupled to anodic oxidation for wastewater treatment: Application to

683 the degradation of acetaminophen, Separation and Purification Technology, 203 (2018) 143-

684 151.

685 [10] I.O. Uribe, A. Mosquera-Corral, J.L. Rodicio, S. Esplugas, Advanced technologies for

686 water treatment and reuse, AIChE Journal, 61 (2015) 3146-3158.

687 [11] M.A. Oturan, J.-J. Aaron, Advanced Oxidation Processes in Water/Wastewater Treatment:

688 Principles and Applications. A Review, Critical Reviews in Environmental Science and

689 Technology, 44 (2014) 2577-2641.

690 [12] G. Ren, M. Zhou, M. Liu, L. Ma, H. Yang, A novel vertical-flow electro-Fenton reactor

691 for organic wastewater treatment, Chemical Engineering Journal, 298 (2016) 55-67.

692 [13] J.A. Zazo, J.A. Casas, A.F. Mohedano, M.A. Gilarranz, J.J. Rodríguez, Chemical Pathway

693 and Kinetics of Phenol Oxidation by Fenton's Reagent, Environ. Sci. Technol., 39 (2005) 9295-

694 9302.

695 [14] E. Brillas, I. Sirés, M.A. Oturan, Electro-Fenton Process and Related Electrochemical

696 Technologies Based on Fenton's Reaction Chemistry, Chem. Rev., 109 (2009) 6570-6631.

697   [15] W. Ren, D. Tang, X. Lu, J. Sun, M. Li, S. Qiu, D. Fan, Novel Multilayer

698   ACF@rGO@OMC Cathode Composite with Enhanced Activity for Electro-Fenton

699   Degradation of Phthalic Acid Esters, Industrial & Engineering Chemistry Research, 55 (2016)

700   11085-11096.

701   [16] W. Wang, Y. Lu, H. Luo, G. Liu, R. Zhang, Effect of an improved gas diffusion cathode

702   on carbamazepine removal using the electro-Fenton process, RSC Advances, 7 (2017) 25627-

703   25633.

704   [17] H. Roth, Y. Gendel, P. Buzatu, O. David, M. Wessling, Tubular carbon nanotube-based

705   gas diffusion electrode removes persistent organic pollutants by a cyclic adsorption – Electro-

706   Fenton process, Journal of Hazardous Materials, 307 (2016) 1-6.

707   [18] P. Su, M. Zhou, X. Lu, W. Yang, G. Ren, J. Cai, Electrochemical catalytic mechanism of

708   N-doped graphene for enhanced H_2O_2 yield and in-situ degradation of organic pollutant,

709   Applied Catalysis B: Environmental, 245 (2019) 583-595.

710   [19] H. Yin, C. Zhang, F. Liu, Y. Hou, Hybrid of Iron Nitride and Nitrogen-Doped Graphene

711   Aerogel as Synergistic Catalyst for Oxygen Reduction Reaction, Advanced Functional

712   Materials, 24 (2014) 2930-2937.

713   [20] C. Lee, X. Wei, Q. Li, R. Carpick, J.W. Kysar, J. Hone, Elastic and frictional properties of

714   graphene, physica status solidi (b), 246 2562-2567.

715   [21] K.-Q. Lu, L. Yuan, X. Xin, Y.-J. Xu, Hybridization of graphene oxide with commercial

716   graphene for constructing 3D metal-free aerogel with enhanced photocatalysis, Applied

717   Catalysis B: Environmental, 226 (2018) 16-22.

718   [22] F. Pan, Y. Duan, X. Zhang, J. Zhang, A Facile Synthesis of Nitrogen/Sulfur Co-Doped

719   Graphene for the Oxygen Reduction Reaction, ChemCatChem, 8 (2016) 163-170.

720   [23] T. Huang, S. Mao, M. Qiu, O. Mao, C. Yuan, J. Chen, Nitrogen-boron Dipolar-doped

721   Nanocarbon as a High-efficiency Electrocatalyst for Oxygen Reduction Reaction,

722   Electrochimica Acta, 222 (2016) 481-487.

723 [24] D. Geng, N. Ding, T.S.A. Hor, Z. Liu, X. Sun, Y. Zong, Potential of metal-free "graphene

724 alloy" as electrocatalysts for oxygen reduction reaction, J. Mater. Chem. A, 3 (2015) 1795-

725 1810.

726 [25] H. Zhang, Y. Niu, W. Hu, Nitrogen/sulfur-doping of graphene with cysteine as a

727 heteroatom source for oxygen reduction electrocatalysis, Journal of Colloid and Interface

728 Science, 505 (2017) 32-37.

729 [26] S.O. Ganiyu, M. Zhou, C.A. Martínez-Huitle, Heterogeneous electro-Fenton and

730 photoelectro-Fenton processes: A critical review of fundamental principles and application for

731 water/wastewater treatment, Applied Catalysis B: Environmental, 235 (2018) 103-129.

732 [27] C.S.D. Rodrigues, O.S.G.P. Soares, M.T. Pinho, M.F.R. Pereira, L.M. Madeira, p-

733 Nitrophenol degradation by heterogeneous Fenton's oxidation over activated carbon-based

734 catalysts, Applied Catalysis B: Environmental, 219 (2017) 109-122.

735 [28] A.I. Zárate-Guzmán, L.V. González-Gutiérrez, L.A. Godínez, A. Medel-Reyes, F.

736 Carrasco-Marín, L.A. Romero-Cano, Towards understanding of heterogeneous Fenton reaction

737 using carbon-Fe catalysts coupled to in-situ H2O2 electro-generation as clean technology for

738 wastewater treatment, Chemosphere, 224 (2019) 698-706.

739 [29] I. Sirés, E. Brillas, M.A. Oturan, M.A. Rodrigo, M. Panizza, Electrochemical advanced

740 oxidation processes: today and tomorrow. A review, Environmental Science and Pollution

741 Research, 21 (2014) 8336-8367.

742 [30] L.M. Pastrana-Martínez, N. Pereira, R. Lima, J.L. Faria, H.T. Gomes, A.M.T. Silva,

743 Degradation of diphenhydramine by photo-Fenton using magnetically recoverable iron oxide

744 nanoparticles as catalyst, Chemical Engineering Journal, 261 (2015) 45-52.

745 [31] W. Chen, X. Yang, J. Huang, Y. Zhu, Y. Zhou, Y. Yao, C. Li, Iron oxide containing

746 graphene/carbon nanotube based carbon aerogel as an efficient E-Fenton cathode for the

747 degradation of methyl blue, Electrochimica Acta, 200 (2016) 75-83.

748   [32] W.S. Hummers, R.E. Offeman, Preparation of Graphitic Oxide, J. Am. Chem. Soc., 80

749   (1958) 1339-1339.

750   [33] L.M. Pastrana Martinez, S. Morales-Torres, V. Likodimos, J. Figueiredo, J. Faria, P.

751   Falaras, A. Silva, Advanced nanostructured photocatalysts based on reduced graphene oxide–

752   TiO_2 composites for degradation of diphenhydramine pharmaceutical and methyl orange dye,

753   Applied Catalysis B: Environmental, 123–124 (2012) 241-256.

754   [34] X. Ren, H. Guo, J. Feng, P. Si, L. Zhang, L. Ci, Synergic mechanism of adsorption and

755   metal-free catalysis for phenol degradation by N-doped graphene aerogel, Chemosphere, 191

756   (2018) 389-399.

757   [35] K. Petcharoen, A. Sirivat, Synthesis and characterization of magnetite nanoparticles via

758   the chemical co-precipitation method, Materials Science and Engineering: B, 177 (2012) 421-

759   427.

760   [36] E. Bailón-García, A. Elmouwahidi, F. Carrasco-Marín, A.F. Pérez-Cadenas, F.J.

761   Maldonado-Hódar, Development of Carbon-ZrO2 composites with high performance as

762   visible-light photocatalysts, Applied Catalysis B: Environmental, 217 (2017) 540-550.

763   [37] E. Gallegos-Suárez, A.F. Pérez-Cadenas, F.J. Maldonado-Hódar, F. Carrasco-Marín, On

764   the micro- and mesoporosity of carbon aerogels and xerogels. The role of the drying conditions

765   during the synthesis processes, Chemical Engineering Journal, 181-182 (2012) 851-855.

766   [38] A. Elmouwahidi, J.F. Vivo-Vilches, A.F. Pérez-Cadenas, F.J. Maldonado-Hódar, F.

767   Carrasco-Marín, Free metal oxygen-reduction electro-catalysts obtained from biomass residue

768   of the olive oil industry, Chemical Engineering Journal, 306 (2016) 1109-1115.

769   [39] A. Abdelwahab, J. Castelo-Quibén, J.F. Vivo-Vilches, M. Pérez-Cadenas, F.J. Maldonado-

770   Hódar, F. Carrasco-Marín, A.F. Pérez-Cadenas, Electrodes Based on Carbon Aerogels Partially

771   Graphitized by Doping with Transition Metals for Oxygen Reduction Reaction, Nanomaterials

772   (Basel, Switzerland), 8 (2018) 266.

773 [40] J. Castelo-Quibén, A. Abdelwahab, M. Pérez-Cadenas, S. Morales-Torres, F.J.

774 Maldonado-Hódar, F. Carrasco-Marín, A.F. Pérez-Cadenas, Carbon - iron electro-catalysts for

775 CO2 reduction. The role of the iron particle size, Journal of CO2 Utilization, 24 (2018) 240-

776 249.

777 [41] S. Brunauer, L.S. Deming, W.E. Deming, E. Teller, On a Theory of the van der Waals

778 Adsorption of Gases, J. Am. Chem. Soc., 62 (1940) 1723-1732.

779 [42] M. Pedrosa, L.M. Pastrana-Martínez, M.F.R. Pereira, J.L. Faria, J.L. Figueiredo, A.M.T.

780 Silva, N/S-doped graphene derivatives and TiO_2 for catalytic ozonation and photocatalysis of

781 water pollutants, Chemical Engineering Journal, 348 (2018) 888-897.

782 [43] X. Wang, G. Sun, P. Routh, D.H. Kim, W. Huang, P. Chen, Heteroatom-doped graphene

783 materials: syntheses, properties and applications, Chemical Society Reviews, 43 (2014) 7067-

784 7098.

785 [44] S. Yang, L. Zhi, K. Tang, X. Feng, J. Maier, K. Müllen, Efficient synthesis of heteroatom

786 (N or S)-doped graphene based on ultrathin graphene oxide-porous silica sheets for oxygen

787 reduction reactions, Advanced Functional Materials, 22 (2012) 3634-3640.

788 [45] V.C. Tung, M.J. Allen, Y. Yang, R.B. Kaner, High-throughput solution processing of

789 large-scale graphene, Nature Nanotechnology, 4 (2009) 25-29.

790 [46] S. Chowdhury, Y. Jiang, S. Muthukaruppan, R. Balasubramanian, Effect of boron doping

791 level on the photocatalytic activity of graphene aerogels, Carbon, 128 (2018) 237-248.

792 [47] L.M. Pastrana-Martínez, S. Morales-Torres, V. Likodimos, P. Falaras, J.L. Figueiredo, J.L.

793 Faria, A.M.T. Silva, Role of oxygen functionalities on the synthesis of photocatalytically active

794 graphene–TiO2 composites, Applied Catalysis B: Environmental, 158-159 (2014) 329-340.

795 [48] J.M. Englert, P. Vecera, K.C. Knirsch, R.A. Schäfer, F. Hauke, A. Hirsch, Scanning-

796 Raman-Microscopy for the Statistical Analysis of Covalently Functionalized Graphene, ACS

797 Nano, 7 (2013) 5472-5482.

798   [49] M.A. Pimenta, G. Dresselhaus, M.S. Dresselhaus, L.G. Cançado, A. Jorio, R. Saito,

799   Studying disorder in graphite-based systems by Raman spectroscopy, Phys Chem Chem Phys,

800   9 (2007) 1276-1291.

801   [50] P. Iamprasertkun, A. Krittayavathananon, M. Sawangphruk, N-doped reduced graphene

802   oxide aerogel coated on carboxyl-modified carbon fiber paper for high-performance ionic-

803   liquid supercapacitors, Carbon, 102 (2016) 455-461.

804   [51] F. Tuinstra, J.L. Koenig, Raman Spectrum of Graphite, The Journal of Chemical Physics,

805   53 (1970) 1126-1130.

806   [52] T. Van Khai, H.G. Na, D.S. Kwak, Y.J. Kwon, H. Ham, K.B. Shim, H.W. Kim, Significant

807   enhancement of blue emission and electrical conductivity of N-doped graphene, Journal of

808   Materials Chemistry, 22 (2012) 17992.

809   [53] L. Chen, X. Cui, Y. Wang, M. Wang, R. Qiu, Z. Shu, L. Zhang, Z. Hua, F. Cui, C. Wei, J.

810   Shi, One-step synthesis of sulfur doped graphene foam for oxygen reduction reactions, Dalton

811   Transactions, 43 (2014) 3420-3423.

812   [54] M. Pérez-Cadenas, C. Moreno-Castilla, F. Carrasco-Marín, A.F. Pérez-Cadenas, Surface

813   Chemistry, Porous Texture, and Morphology of N-Doped Carbon Xerogels, Langmuir, 25

814   (2009) 466-470.

815   [55] C. Zhang, R. Hao, H. Liao, Y. Hou, Synthesis of amino-functionalized graphene as metal-

816   free catalyst and exploration of the roles of various nitrogen states in oxygen reduction reaction,

817   Nano Energy, 2 (2013) 88-97.

818   [56] Z.-S. Wu, W. Ren, L. Xu, F. Li, H.-M. Cheng, Doped Graphene Sheets As Anode Materials

819   with Superhigh Rate and Large Capacity for Lithium Ion Batteries, ACS Nano, 5 (2011) 5463-

820   5471.

821   [57] Z. Yang, Z. Yao, G. Li, G. Fang, H. Nie, Z. Liu, X. Zhou, X.a. Chen, S. Huang, Sulfur-

822   Doped Graphene as an Efficient Metal-free Cathode Catalyst for Oxygen Reduction, ACS

823   Nano, 6 (2012) 205-211.

824 [58] A. Elmouwahidi, J. Castelo-Quibén, J.F. Vivo-Vilches, A.F. Pérez-Cadenas, F.J.

825 Maldonado-Hódar, F. Carrasco-Marín, Activated carbons from agricultural waste

826 solvothermally doped with sulphur as electrodes for supercapacitors, Chemical Engineering

827 Journal, 334 (2018) 1835-1841.

828 [59] X. Liu, M.D. Kaminski, Y. Guan, H. Chen, H. Liu, A.J. Rosengart, Preparation and

829 characterization of hydrophobic superparamagnetic magnetite gel, Journal of Magnetism and

830 Magnetic Materials, 306 (2006) 248-253.

831 [60] J. Zhang, H. Zhou, X. Liu, J. Zhang, T. Peng, J. Yang, Y. Huang, S. Mu, Keratin-derived

832 S/N co-doped graphene-like nanobubble and nanosheet hybrids for highly efficient oxygen

833 reduction, J. Mater. Chem. A, 4 (2016) 15870-15879.

834 [61] J. Zhu, K. Li, M. Xiao, C. Liu, Z. Wu, J. Ge, W. Xing, Significantly enhanced oxygen

835 reduction reaction performance of N-doped carbon by heterogeneous sulfur incorporation:

836 synergistic effect between the two dopants in metal-free catalysts, J. Mater. Chem. A, 4 (2016)

837 7422-7429.

838 [62] A. Elmouwahidi, E. Bailón-García, A.F. Pérez-Cadenas, J. Castelo-Quibén, F. Carrasco-

839 Marín, Carbon-vanadium composites as non-precious catalysts for electro-reduction of oxygen,

840 Carbon, 144 (2019) 289-300.

841 [63] K. Gong, F. Du, Z. Xia, M. Durstock, L. Dai, Nitrogen-Doped Carbon Nanotube Arrays

842 with High Electrocatalytic Activity for Oxygen Reduction, Science, 323 (2009) 760-764.

843 [64] T.X.H. Le, T.V. Nguyen, Z. Amadou Yacouba, L. Zoungrana, F. Avril, D.L. Nguyen, E.

844 Petit, J. Mendret, V. Bonniol, M. Bechelany, S. Lacour, G. Lesage, M. Cretin, Correlation

845 between degradation pathway and toxicity of acetaminophen and its by-products by using the

846 electro-Fenton process in aqueous media, Chemosphere, 172 (2017) 1-9.

847